Antiferromagnetism, Anion Disorder, and Lattice Defects in the S = 5/2 [Bi2O2][Mn2+F4] Aurivillius Compound

Jonas Wolber, Victor Duffort, Delphine Filipiak, Xavier Rocquefelte, Marielle Huvé, Theodosios Famprikis, Angel Arévalo-López, Oscar Fabelo, Olivier Mentré

Antiferromagnetism, Anion Disorder and Lattice Defects in the *S*=5/2 $[Bi_2O_2][Mn^{2+}F_4]$ Aurivillius Compound

Jonas Wolber[1,2], Victor Duffort[1], Delphine Filipiak[1], Xavier Rocquefelte[3], Marielle Huvé[1], Theodosios Famprikis[4], Ángel-M. Arévalo-López[1], Oscar Fabelo[2], Olivier Mentré[1,*]

[1] UCCS (Unité de catalyse et chimie du solide) - Axe Chimie du Solide, UMR-CNRS 8181, Ecole Centrale/Université de Lille, F-59655 Villeneuve d'Ascq, France
[2] ILL (Institut Laue-Langevin), F-38042 Grenoble, France
[3] Université de Rennes, ISCR (Institut des Sciences Chemiques de Rennes) - UMR-CNRS 6226, F-35042 Rennes, France
[4] Department of Radiation Science and Technology, Faculty of Applied Sciences, Delft University of Technology, 2629 JB Delft, the Netherlands
[*] Corresponding author, Email: Olivier.mentre@univ-lille.fr

Abstract:

$[Bi_2O_2][MnF_4]$ is a novel Aurivillius oxyfluoride with Mn^{2+} cations filling the one-layer perovskite sub-units. Its synthesis as single-phase material by high-temperature solid state route is complicated by the high volatility of fluorine in the used precursors and by its limited thermal stability above 400°C. Its crystal structure was determined using synchrotron and neutron diffraction data. It shows structural singularities, highlighted by the anion positional disorder inherent to the *I*4/*mmm* space group, despite the evidence of strong local axial and equatorial octahedral tilts along with clues for ideal F^- and O^{2-} total segregation in the two layered subunits. Contrarily to the M = Ni^{2+}, Co^{2+}, $Fe^{2+/3+}$ analogs where similar tilts order in various supercells, for M = Mn^{2+} only short-range ordering (SRO) was detected by electron diffraction. This was rationalized in terms of the d^5 ion isotropic nature, for which weak distortions of the crystal-field do not have an energy penalty and favor local octahedral defects acting as antiphase boundaries between nanometric SRO domains. DFT calculations validate equiprobable tilted $[MnF_6]$ arrangements in the perovskite layers and suggest the possibility for O↔F exchange in between the $[Bi_2O_2]$ and $[MnF_4]$ modules, supported by HAADF imaging. The presence of oxygen and vacancies in the perovskite slabs was also detected on samples prepared at higher temperature. $[Bi_2O_2][MnF_4]$ magnetic structure shows a colinear antiferromagnetic arrangement below T_N = 19.8 K, with Mn^{2+} spins (*S*=5/2, *L*=0) aligned parallel to the *c*-axis (M_z = 3.8(2) μ_B/Mn). This is again in contrast with the systematic spin-canting responsible for weak ferromagnetism in the previous M^{2+} Aurivillius compounds. Finally, modest fluoride ionic mobility was measured in a small temperature range, restricted by the stability of the compound in air.

Introduction:

Today, compounds with multiple anions beyond the single-oxide ion, are recognized as a new sizeable materials platform from which superior functionality may arise.[1] In that frame the inorganic oxyfluoride materials emerge among the various generic families such as oxynitrides, oxyhydrides, oxychalcogenides, and oxyhalides. This particular positioning relies on the O^{2-} and F^- similar ionic size, but different charge, electronegativity, hardness, and polarizability. It allows for versatile building of mixed anionic networks influenced by the selected M cation and resulting in distinct sub-units from fully disordered to fully ordered O/F segregated motifs. As a general principle, the oxyfluoride structural edifice operates with more ionic M-F bonds and more covalent M-O bonds due to the superior charge and polarizability of oxide anions.[2] In this frame, the Aurivillius oxyfluorides emerge as intriguing modifications of the parent, layered ferroelectric compounds. Indeed, starting from their modular developed formula $(Bi_2O_2)_{fluorite}(A_{n-1}M_nO_{3n+1})_{perovskite}$, the incorporation of F^- anions in the perovskite slabs was shown to allow for the stabilization of stoichiometric n = 1 members with M transition metal in an oxidation state lower than +6, usually found in the $(Bi_2O_2)(M^{6+}O_4)$, M = Mo, W aristotypes.

It results in phases such as $(Bi_2O_2)((Nb/Ta/V)^{5+}O_3F)$ and $(Bi_2O_2)(Ti^{4+}O_2F_2)$.[3–5] These compounds are thought to be ferroelectric due to the combination of the lone pair active, asymmetric Bi^{3+} ions and second-order Jahn-Teller effect of d^0 M^{n+} ions in the $[Bi_2O_2]$ and perovskite slabs respectively. However, they display tetragonal lattices with O/F mixed and split positions, making it difficult to get the experimental evidence of a genuine ferroelectric behavior. Consequently, in the most studied $(Bi_2O_2)(Ti^{4+}O_2F_2)$ compound, experimental evidences in the search for dielectric and ferroelectric features are controversial [5–8] and suggest sample-dependent properties. Surprisingly, an antiferroelectric behavior, *i.e.*, transitioning from a non-polar to a polar phase under an electric field, was recently demonstrated for $(Bi_2O_2)(Ti^{4+}O_2F_2)$. This structural change is governed by an original mechanism involving the rotation of the $[TiO_3F_3]$ octahedra within the perovskite layers. The resulting shifts of O^{2-} and F^- ions along the *c*-axis are often different in magnitude and correlated to their different valence. [9] At least from DFT, $O_{equatorial}/F_{apical}$ ordered polar domains can plausibly be expected. During the search for O/F ordering, via experimental and theoretical studies,[5,6,10] the higher stability for apical F^- in the perovskite layers was demonstrated by DFT. Recently, a significant step forward was achieved by the preparation of Aurivillius oxyfluorides with paramagnetic $3d^n$ ions with the $(Bi_2O_2)(M^{2+}F_4)$ ideal formula and M = Fe, Co, Ni.[11–13] They all show canted antiferromagnetism and evidence of ordered polar supercell symmetry. In this context, a polar lattice was proved by second harmonic generation for M = Fe and Co. In the former, multiferroic $(Bi_{2-x}O_2)(Fe^{2+/3+}F_4)$ compound, multiferroic behavior has been effectively measured via electric polarization, it further shows weak ferromagnetism, and magnetoelectric coupling.[11] This occurs despite the increased ionic character of the fluorides compared to the oxides which is expected to reduce the stability of polar distortions. In addition, in both of these compounds, mixed valent $M^{2+/3+}$ was suggested due to anionic vacancies and possible mixed O/F occupancies (M = Co) and/or Bi vacancies (M = Fe) in the perovskite and fluorite sub-units respectively. The mixed $Fe^{2.5+}$ valence was confirmed in the bulk by Mössbauer spectroscopy,[11] but the effective valence seems to depend on the synthesis conditions.

Here we report on the successful incorporation of M = Mn^{2+} ions with the highest available $S = 5/2$ spin in the original $(Bi_2O_2)(MnF_4)$ compound. In the context of a fully disordered tetragonal crystal structure, we analyzed the origin of the single Mn^{2+} valence rather than mixed valence from the inspection of various plausible lattice defects, the assistance of the d^5 crystal-field on the observed structure, and the analysis of the magnetic and transport properties.

Experimental:

***XRPD*:** Room temperature X-ray powder diffraction (XRPD) is carried out using a Bruker D8 Advance in Bragg-Brentano geometry (Cu-K_α).

***SXRD*:** Synchrotron X-ray powder diffraction (SXRD) with high angular resolution is collected on the BL04-MSPD beamline (λ = 0.41 Å) in an angular range from 0.5° to 34° at the Alba synchrotron in Barcelona.

***NPD*:** Low and room temperature neutron powder diffraction (NPD) patterns are recorded with the PEARL diffractometer (λ = 1.67 Å) at the Reactor Institute of the Delft University of Technology.[14] The powder sample is loaded in a null-scattering-alloy can. Diffraction patterns are collected using a wavelength of 1.67 Å selected using a single-crystal Ge monochromator. For the room-temperature measurement, the sample can is placed in a neutron-transparent vacuum box connected to a primary vacuum (~ 10^{-3} mbar). For low temperature measurements at 30 and 5 K a liquid-helium cryostat is used. An additional room temperature measurement is carried out on the D2B (λ = 1.59 Å) beamline of the Institut Laue-Langevin (ILL) in Grenoble. Both are used to record high resolution data for accurate structure refinements.

***Data analysis and presentation*:** Powder diffraction data is refined by the Rietveld method in Fullprof (V7.30). Stacking faults are considered using the FAULTS program [15] included in

Fullprof. Plots are created in Origin 2021b. Pictures of crystal structures are prepared in Diamond (V4.5.1).

***TGA(-MS)*:** Thermogravimetric analysis coupled to mass spectroscopy (TGA-MS) is conducted on a TGA-92 thermobalance (Setaram) under synthetic air (80%/20% N_2/O_2) and pure nitrogen. The relative humidity of the carrier gases is adjusted to ~ 20% RH @25°C, corresponding to a dew point of ~ 1°C, using a WetSys (Setaram) humidity controller. The evolved gases are monitored by an Omnistar quadrupole mass spectrometer (Pfeiffer). The samples are heated to 800°C at a rate of 1 K min^{-1}.

***Magnetic measurements*:** For the magnetic measurements a Quantum Design PPMS 9T DynaCool is used. Zero field cooled (ZFC) data is recorded, after cooling down the sample without an external magnetic field, on heating in an external field of 0.1 T. The field cooled (FC) data then is recorded in the same external field on cooling.

***TEM*:** A FEI Tecnai G2-20 twin (200kV) transmission electron microscope (TEM) is used to do selected area electron diffraction (SAED) on selected particles of the powder to confirm the unit cell refined from powder diffraction. Scanning transmission electron microscopy (STEM) analysis was conducted using a high-base Titan Themis 80-300 S/TEM equipped with a Super-X four-quadrant silicon drift detector for energy dispersive X-ray spectroscopy (EDX), a high-brightness Schottky field emission gun (X-FEG), a probe aberration corrector, and a Wien filter monochromator. This setup was chosen since it provides an optimal spatial resolution of 70 pm, precise electron dose control in non-filtered mode, and a possible energy resolution down to 150 meV in filtered mode. The microscope was also fitted with a direct electron detector (256x1024 pixel four-quadrant Medipix) installed behind a GATAN post-column high-resolution energy filter (Quantum ERS/966). In all the electron microscopy experiments, the microscope was operated at 300 kV. High-angle annular dark-field imaging (HAADF) allows capturing of pictures with atomic resolution. Energy dispersive X-ray spectroscopy (EDX) permits elemental analysis. Electron energy loss spectroscopy (EELS) is used to estimate the oxidation state of Mn.

***EIS*:** Ionic mobility is evaluated on cylindrical pellets of Sample B. Gold electrodes were sputtered on the circular surfaces of the ceramic sample, which was mounted via a pseudo-4-wire setup on a custom high-temperature rig. Complex electrochemical impedance spectra (EIS) are collected in air every 25°C in the 150 – 400 °C temperature range via a Solartron 1260 frequency response analyzer (FRA), which measures 71 points logarithmically spaced across the 1 MHz to 100 mHz frequency range using an excitation AC voltage of 500 mV. The EIS spectra are fitted to equivalent electrical circuits with the EC-Lab software (Biologic).

***DFT calculations*:** Theoretical calculations were performed within Density Functional Theory (DFT) using the Vienna Ab initio Simulation Package (VASP).[16–18] The Generalized Gradient approximation (GGA) with Perdew-Burke-Ernzerhof (PBE) functional was employed for electron exchange and correlation.[19] Atom cores are described through the projector augmented wave (PAW) method.[20] The kinetic energy cutoff for plane wave expansions was set to 500 eV for all calculations. Atomic positions were optimized until forces were converged to lower than 10^{-3} eV/Å. Since the localized 3*d* states of Mn are not properly treated in DFT, a Hubbard U correction has been added using the GGA+U method [21] with $U_{eff} = U - J = 4$ eV.

Both atomic positions and cell parameters have been optimized for the ideal models (*A*2/*a* and *P-1*) using a spacing of 0.2 $Å^{-1}$ for the Brillouin zone sampling and a *G*-type antiferromagnetic order of the Mn magnetic moments.

The defect models have been created using a 2×2×1 supercell of the *ideal A*2/*a* model. Only the atomic positions have been relaxed for these models using a Monkhorst-Pack mesh of 1x1x1 for the Brillouin zone sampling.[22]

***Synthesis*:** BiOF (97%, Thermo Scientific) and MnF_2 (99%, Alfa Aesar) were used as the starting materials. Our solvothermal tests using dilute HF within conditions similar to what is used for M = Co and Fe failed and mainly show unreacted MnF_2 and various bismuth oxyfluoride products. Alternatively, high temperature solid state reaction between BiOF (2 Eq.) and MnF_2 (1 Eq.) pressed into pellets and sealed in evacuated silica tube was tested in several conditions. Sizeable amounts of elemental Bi, MnF_2, and SiO_2 are most often found as co-products. The best results were obtained at 700°C for 72h in a single heating step (Sample A), used for neutron powder and synchrotron X-ray diffraction (NPD and SXRD) and magnetic properties. Note that many parameters such as the Bi:Mn ratio, the amount of sample, and additional re-grinding or re-heating steps can be detrimental to the final purity without clear rationalization. Large amount of SiO_2 was systematically found in the final product, caused by a chemical vapor transport (CVT)-like volatilization promoted by fluorine-based transport agent. Our attempts to confine the reactant in slightly-opened gold tubes, alumina crucibles or using carbon coated silica did not avoid this issue, and even reactions at 450°C show large amount of SiO_2 recondensed in the phase. Alternatively, we used high frequency induction heating inside a tantalum tube (inductor heated around 750°C) itself placed in an evacuated quartz tube. In this manner, the quartz being kept close to room temperature, samples did not find any trace of SiO_2, but even after several re-grinding/re-heating steps, we found traces (few weight percent) of Mn_3O_4 or MnF_2 which mask the intrinsic magnetic response of the sample (Sample B, used for thermal analyses and impedance spectroscopy). In such conditions the size of the batches is limited to ~ 0.5 g to maintain compositional homogeneity. In addition, after several uses, the Ta tube starts to react and the syntheses of large batches show inhomogeneous products (sample C, used for a complementarily neutron powder experiment). For these reasons, it was difficult to perform our analyses using a unique sample and our choice was adapted to the respective measurement requirements in terms of sample-size and amount as well as nature of the impurities.

Disorder over a stoichiometric Crystal structure:

A sample-A type batch with 76 wt.% of purity ($Bi_2MnO_2F_4$ 76 wt.%, $SiO_{2\text{-trigonal}}$ 21 wt.%, Bi^0 1.2 wt.%, BiOF 1.2 wt.%, $SiO_{2\text{-tetragonal}}$ 1.6 wt.%) prepared in a heated silica tube was used. It was analyzed by Rietveld refinement using both synchrotron X-ray diffraction (SXRD, R_{Bragg}=7.8%), and neutron-powder diffraction data (NPD, R_{Bragg}=1.91%) as shown in Fig.1a. It was refined in the tetragonal cell a_p = 3.87174(3) Å, c = 16.7568(2) Å against SXRD data, with the space group: *I*4/*mmm*. The a_p label relates to the simple perovskite lattice. Additional information on the structure refinement are given in the supporting information (Table S1-3). All diffraction techniques show no evidence of any ($\sqrt{2}\cdot a_p$, $\sqrt{2}\cdot a_p$, c) orthorhombic supercell, commonly observed in other Aurivillius oxyfluorides. This latter would arise from the in-plane and equatorial tilted organization of the [MX_6] octahedra, whose disordered fingerprint is observed by the important four-fold split of all 1/4th occupied anions inside the perovskite slabs, see Fig.1e. The subcell is highlighted on selected area electron diffraction (SAED), see Fig.1b and c.

In the M = $Fe^{2+/3+}$ [11] and Co^{2+} [12,13] Aurivillius O/F compounds, Bi-vacancies and mixed O/F/vac. occupancies were respectively suggested. In contrast, here, despite the large refined F thermal parameters, after trying to refine all site-occupancies, the best refinements were achieved for the ideal $[Bi_2O_2][MnF_4]$ stoichiometry. It is in tune with our EDX spectroscopy in various samples which returned Bi:Mn 2.0:1.0 and F:O 2.3:1.0 ratios. Taking into account the weak O/F scattering contrast in both NPD and XRD techniques, the ideal O/F segregation in the fluorite and perovskite slabs respectively is suggested by *i*) bond valence sum calculations (BVS[$F_{equ.}$/$F_{apic.}$] = -0.76/-0.64 (F^- hypothesis) *vs.* -0.93/-0.44 (O^{2-} hypothesis) ; BVS[O] = -2.27 (O^{2-} hypothesis) *vs.* -1.72 (F^- hypothesis) ; BVS[Bi] = +2.60

(Bi^{3+}-O^{2-} hypothesis) ; BVS[Mn] = +2.22 (Mn^{2+}-F^{-} hypothesis) using BVS parameters from Brese and O'Keeffe [23] and *ii*) EELS results which suggest a single Mn^{2+} valence. The average Mn-Mn distances of ~ 3.87 Å and Mn-F-Mn angles of ~ 133-138° can be deduced from such disordered model, using the most regular octahedra shown in Fig.1f-h. However, on the [010] zone axis diffraction pattern, an incommensurate modulation vector $\vec{q}_1 \sim 0.88\ \vec{a}^*$ is observed, but the very weak satellite spots suggest short-range correlations only. These satellites have not been observed by SXRD nor NPD.

We note that another NPD experiment on a larger sample C, prepared in a high frequency induction heater (T = 650 – 700 °C) and although largely contaminated by by-products ($Bi_2O_2MnF_4$ 55.2 wt.%, $Bi_{1.75}MnTaO_{6.62}$ 20.2 wt.%, MnF_2 17.5 wt.%, Bi_2O_3 5.3 wt.%, Mn_3O_4 1.7 wt.%) returns a similar result, see Fig.S1.

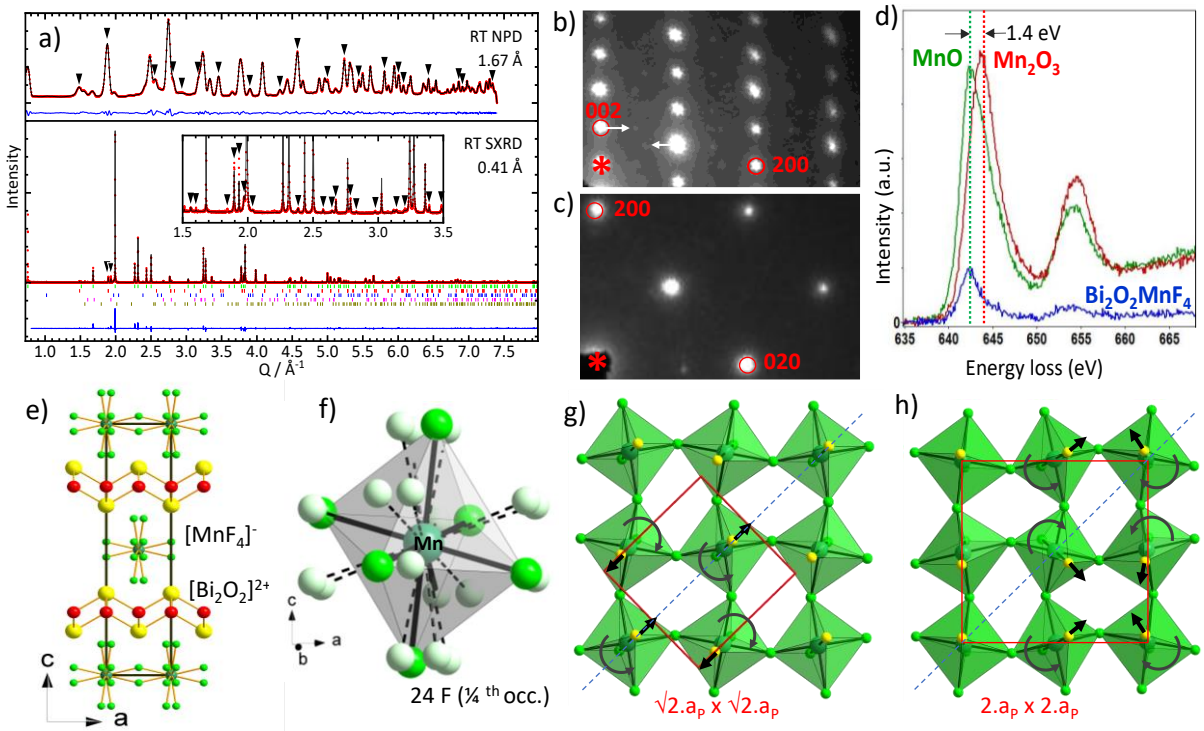

Figure 1: $Bi_2O_2MnF_4$. a) Room temperature neutron (PEARL diffractometer (λ = 1.67 Å)) and synchrotron powder diffraction (ALBA BL04-MSPD (λ = 0.41 Å)) Rietveld refinements. The inset shows the small impurity reflections in the SXRD diffractogram marked with black triangles. b) [010] zone axis selected area electron diffraction (SAED) pattern with weak supercell spots indicated with white arrows. c) [001] zone axis SAED pattern. d) EELS spectrum of the Mn-$L_{3,2}$ edge. e) Unit cell of the refined crystal structure. f) MnF_6 coordination. In grey one "ideal" of four due to octahedral tilting superimposing octahedra is shown. g) $ideal_{A2/a}$ and h) $ideal_{P\text{-}1}$ tilting schemes of the octahedra in the perovskite layers (green) as used for DFT.

Thus, our results also agree with the well-known superior thermal stability of MnF_2 compared to MnF_3. The latter being stable at ambient conditions, but releasing fluorine upon heating and finishing in MnF_2.[24]

Although the refined full stoichiometry avoids mixed valence and vacancy issues, it nevertheless raises questions about the origin of its apparent disordered tetragonal lattice. Indeed, our compound escapes the mixed O/F perovskite topology enforced by higher metal valences such as in the M = Ti^{4+}, V^{5+}, Nb^{5+}, Ta^{5+} Aurivillius compounds mentioned in the introduction. However, the lack of long-range ordering (LRO) in the experimental subcell suggests the presence of local anionic defects, acting as anti-phase boundaries between various short-range-ordered (SRO) domains. The inspection of HAADF images of the *ac* plane is informative (Fig.2). In most of the examined thin areas, the stacking between the layers is regular in terms of *d*-spacing but often shows irregular dark/light contrast along rows parallel to the *a*-axis. A contribution of irregular crystal thickness parallel to the electron-beam is plausible. However, the $[MnF_4]$ slabs are sensitively more affected than the $[Bi_2O_2]$ ones, as

graphically highlighted with the integrated intensities along the lines. The central Mn row shown in Fig.2b, exhibits an undulation period which seems to be random along the *a*-axis (width of 11 and 6 cells indicated in Fig.2b) but maybe related to the overall $\vec{q}_2 \sim 0.44\ \vec{a}^*$ weak modulation observed on the corresponding SAED pattern, doubled in real space from the observed SAED $\vec{q}_1$ value. Assuming a regular Mn alignment but a variation of the F^- position along the viewing direction, one can expect more or less constructive F/Mn interfering waves. From the $\vec{q}_2$ value (0.44 ~ 7/16) one could also imagine short-range periods of ~ 16 unit cells, achieving a pseudo-order of tilted MnF_6 octahedra.

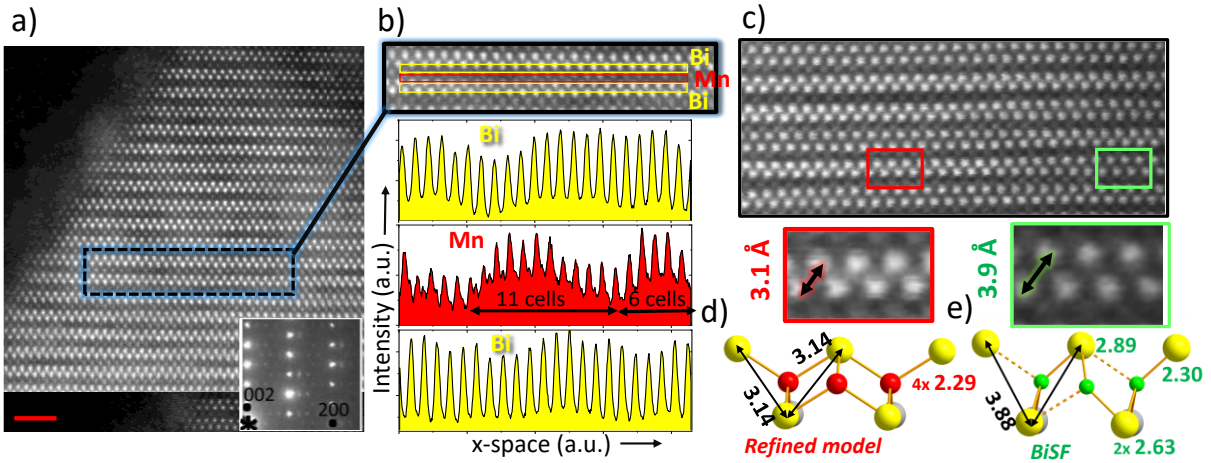

Figure 2: $Bi_2O_2MnF_4$. a) Most representative HAADF images of the *ac* plane with contrasted intensities along lines and corresponding SAED pattern. b) Undulation of the contrast along one Mn and the next two Bi layers. c) Specific HAADF images with undulations of the atomic lines associated to sizeable differences in the projected Bi-Bi distances. d) Analogy of the Bi-Bi distances with the refined model ($[OBi_4]$ tetrahedra) and e) BiSF structure ($[FBi_{3+1}]$ tetrahedra).[25]

Investigation of the anionic disorder:

In such disordered context, we have investigated the most plausible lattice or stacking defects using diffraction experiments, HAADF images, and first-principle calculations.

Inter-planar decoherence: A plausible scenario would be the loss of coherence of perfectly ordered layers across the $[Bi_2O_2]^{2+}$ spacers, resulting in a random stacking. This was tested using the FAULTS program, [15] stacking only the $ideal_{A2/a}$ layers (see Fig.1g) with eight possible stacking types across the central $[Bi_2O_2]^{2+}$ spacer in between the layers with equiprobabilities, see Fig.S3. In this model, the Bi, Mn and O positions fully respect the *I*4/*mmm* symmetry such that the diffuse scattering is solely generated by the F^- sublattice. As expected, the faulted versus ideal SXRD patterns are similar. Conversely, significant alteration of the NPD patterns occurs at specific diffraction angles, see Fig.S3. The comparison with our polynomial-fitted background did not match, except from the (too) large background peak around $2\theta = 40°$ ($Q = 2.7\ Å^{-1}$). In addition, in one pseudo-turbostratic-like situation conserving the *d*-spacing along *c**, one expects large in plane diffuse streaks in the [010] ED patterns, which are not observed, see Fig.1b. As a partial conclusion, we suggest that the main structural decoherence occurs in-plane via slight $[MnF_6]$ local distortions rather than in between planes. This allows for the copresence of differently twinned domains with low energy penalties. On average, each Mn site appears surrounded by eight equiprobable tilted $[MnF_6]$ octahedra.

In-plane Disorder: This scenario was examined by DFT. In order to skirt the issues of $1/4^{th}$ occupied F positions, two plausible fully ordered tilted models have been built using distinct arrangements of a single "*most-regular*" $[MnF_6]$ octahedron with various tilting sequences. The corresponding perovskite sub-units are shown in Fig.1g,h and labeled according to the resulting

crystal symmetry: "*ideal*$_{A2/a}$" (**unit cell**: $\vec{a}' = \vec{a}_p + \vec{b}_p$, $\vec{b}' = -\vec{a}_p + \vec{b}_p$, $\vec{c}' = \vec{c}$) and "*ideal*$_{P\text{-}1}$" (**unit cell**: $\vec{a}' = 2\vec{a}_p$, $\vec{b}' = 2\vec{b}_p$, $\vec{c}' = (-\vec{a}_p - \vec{b}_p + \vec{c}_p)/2$).

As a preamble, the 10 Dq crystal field energy splitting of a d^5 Mn^{2+} ion, does not stabilize any robust [MnF_6] geometry. Therefore, in a simple approach, costless [MnF_6] local distortions are plausible and may play as local "*scissors*" between SRO micro-twinned domains. Such in-plane disorder scenario was unraveled by comparing the energies of both fully ordered *ideal*$_{A2/a}$ *and ideal*$_{P\text{-}1}$ structures after structural relaxation by DFT+U calculations (U = 4 eV). It should be noticed that the optimized cell parameters of both models are in very good agreement with the experimental ones, with deviations smaller than 1% and 2% for the *ideal*$_{A2/a}$ and *ideal*$_{P\text{-}1}$ symmetries, respectively, validating our DFT+U approach (Table S5). The difference in energy between both models is as little as $\Delta E \sim 20$ meV/f.u., which reasonably validates equiprobable sequences of tilted octahedra. So, the in-plane intergrowth between variously-tilted domains is costless from an energy point of view, and may represent the main reason for the disordered crystal structure. In this scenario distortions out of the "most regular" [MnF_6] geometry are expected at the interfacial boundary. In addition, the absence of diffuse scattering in the [010] and [001] zone axes' ED patterns suggest pronounced disorder with ordering ranges between regular octahedral sequences lower than the standard coherence length of hundreds of nanometers for electron microscope studies.

Local Lattice defects: Off-stoichiometry in both the anionic and cationic sublattices and anti-site O/F disorder have been proposed in most of the Aurivillius oxides [26] and oxyfluorides.[10] For energetical ranking, we have calculated by DFT+U the energy of various lattice defects. In case of creation or consumption of Bi, O, F vacancies compared to the [Bi_2O_2][MnF_4] ideal stoichiometry, we have computed and used the energy of $O_{2(g)}$, $F_{2(g)}$, and $Bi_{(s)}$ to estimate the enthalpy of formation for the defects. We have used a 2×2×1 supercell of the *ideal*$_{A2/a}$ model ($V_{defects} \sim 11\times11\times16$ Å^3) to allow for isolated single defects, thus minimizing defect-defect interactions. Our simulated defects are either redox-active or redox-inactive depending on the change of the ideal Mn^{2+} starting valence. It should be noted that the so-obtained defect formation energies may significantly change under the synthesis conditions (or chemical atmosphere). Properly taking into account these aspects would require to determine the stability domain of $Bi_2O_2MnF_4$ in terms of chemical potentials, which is not trivial for a quaternary compound and is out of the scope of the present article. Our results will thus provide qualitative tendencies that may be improved in the future. However, if present, the ratio of computed defects should be out of the precision of our diffraction fits, from which the ideal stoichiometry was refined.

a) redox-active defects: The replacement of both *i*) $F_{equatorial}$ and *ii*) F_{apical} by oxygen slightly increases the Mn oxidation state at the supercell scale. However, *iii*) the creation of a Bi-vacancy, creates a strongly oxidizing situation (loss of $3e^-$ per V_{Bi}). Therefore, oxidation of the sample is more likely to occur through the creation of bismuth vacancies (2.62/3 = 0.87 eV/(e^- 16f.u.)) rather than oxygen incorporation (1.90 – 2.23 eV/(e^- 16f.u.)).

b) redox-inactive defects: Five charge-neutral defects were examined, three of them being related to the creation of a Bi^{3+} vacancy together with three F^- vacancies in various positions more or less close to V_{Bi}. The fourth one involves an O↔F_{ap} exchange. We also investigated the modification of a Mn coordination after exchanging one apical F^- for O^{2-} and creation of a F^- vacancy in its equatorial coordination.

c) Results: The energetical results and main structural changes are listed in Table 1. The relaxed structures, focusing on the defected-slabs are shown in Fig.S6. In short, the highest energy

configurations concern defects associated with creation of vacancies in the perovskite anionic sublattice. Especially, ~ 12 eV/16f.u. were calculated for the creation of three F^- vacancies together with one Bi^{3+} vacancy. This result appears mainly independent of the distribution of V_F in the layers, which proves a labile anionic reorganization after relaxation. This large energy contrasts with the 2.62 eV calculated for V_{Bi} only (redox-active), which moderates the energy associated with the mild Mn oxidation. Here we recall the prior observation of large Bi-deficiency in $Bi_{2-x}O_2FeF_4$ (~ 10%)[11] and $Bi_{2-x}O_2VO_{4-x}$ (~ 10%).[26]

The creation of a single anionic vacancy and one O^{2-} for F^- exchange (5.06 eV) is more stable but highlights the high energy cost related to the final concentration of anionic vacancies.

The most stable calculated defect is redox-inactive and concerns the F↔O site exchange and induces a shift of the Bi atoms away from the alien F^- in the Bi_2O_2-layer creating strongly distorted $[FBi_{3+1}]$ (3x2.4 Å + 1x2.7 Å) anti-tetrahedra instead of regular $[OBi_4]$ (4x2.3 Å) in the parent one. Its energy of 0.6 eV is significantly more stable than the ones of the redox-active O^{2-} for F^- substitution (1.90 and 2.23 eV) which validates the Mn^{2+} preference in fluoride-rich coordination. The incorporation of oxygen in the apical sites of the octahedra is more feasible than in the equatorial ones.

Indirect evidences of such defects have been observed on some specific HAADF images at the thin crystal edges, see Fig.2c. Strong out-of-phase undulation of the $[Bi_2O_2]$ and $[MnF_4]$ layers thickness is observed. The most significant changes concern the former layers in which (Bi-Bi) projected distances range between 3.1 Å and 3.9 Å in the "stressed" and "stretched" segments. Such drastic Bi shifts are reminiscent of what is observed previously for the $[O↔F_{ap.}]$ defect calculation. In Fig.2d,e, we compare the in-plane projected Bi-Bi distances in standard OBi_4 (*e.g.* Aurivillius) and less common $[FBi_{3+1}]$ (*e.g.* BiSF)[25] anti-tetrahedra. The matching strongly suggests the reality of F^- incorporation into the fluorite layers. However, it is expected to remain very limited, since we did not find evidences of such strongly displaced oxygen sites on Fourier-difference maps in our NPD refinements.

Table 1: $Bi_{2-x}O_2MnF_{4-y}$. Effect of O/F disorder or vacancies calculated by DFT+U (U_{eff} = U - J = 4 eV) energies and structural changes compared to the ideal $Bi_2O_2MnF_4$ composition are reported for the 16-fold supercell.

Description	Formula per cell	Mn valence	E/eV	Comment/defect geometry
parent phase	$(Bi_2O_2Mn_1F_4)_{16}$	+2	0	Mn-F=2.1 Å Bi-O=2.3 Å Bi-F_{api}=2.4 Å-3.4 Å Mn-Mn=3.9 Å ∠F_{api}-Mn-F_{api}=180° ∠F_{eq}-Mn-F_{eq}=180°
1 O ↔ 1 F_{api}	$(Bi_2O_{31/16}F_{1/16}Mn_1F_{63/16}O_{1/16})_{16}$	+2 redox-inactive	0.60	Mn-O_{api}=2.1 Å Bi-$F_{in\ O\ layer}$=2.4 Å-2.7 Å 2x Bi-O_{api}=2.2 Å
1 O → 1 F_{api}	$(Bi_2O_2Mn_1F_{63/16}O_{1/16})_{16}$	+2.0625 redox-active	1.90	Mn-O_{api}=1.8 Å Mn-F=2.0 Å-2.1 Å 1x Bi-O_{api}=2.3 Å
1 O → 1 F_{equ}	$(Bi_2O_2Mn_1F_{63/16}O_{1/16})_{16}$	+2.0625 redox-active	2.23	Mn-O_{api}=1.8 Å-2.1 Å Mn-F=2.0 Å-2.2 Å Mn-$Mn_{via\ O}$=3.6 Å
1 $V_{Bi\text{-}site}$	$(Bi_{31/16}O_2Mn_1F_4)_{16}$	+2.1875 redox-active	2.62	∠F_{api}-Mn-F_{api}=169°-172° Bi-$O_{close\ to\ VBi}$=2.2 Å
1 O → 1 F_{api} + 1 $V_{F\text{-}eq}$	$(Bi_2O_2Mn_1F_{62/16}O_{1/16})_{16}$	+2 redox-inactive	5.06	Mn-O_{api}=2.0 Å ∠O_{api}-Mn-F_{api}=147° Mn-$Mn_{via\ VF}$=4.1 Å
1 V_{Bi} + 3$V_{F,around\ VBi}$	$(Bi_{31/16}O_2Mn_1F_{61/16})_{16}$	+2 redox-inactive	11.84	Bi-$O_{close\ to\ VBi}$=2.2 Å ∠F_{api}-Mn-F_{api}=160°-178° ∠F_{eq}-Mn-F_{eq}=155°-168°
1 V_{Bi} +3$V_{F,random}$	$(Bi_{31/16}O_2Mn_1F_{61/16})_{16}$	+2 redox-inactive	12.16	Bi-$O_{close\ to\ VBi}$=2.2 Å ∠F_{api}-Mn-F_{api}=151°-178° ∠F_{eq}-Mn-F_{eq}=169°-174°
1 V_{Bi} + 3$V_{F\text{-}api}$	$(Bi_{31/16}O_2Mn_1F_{61/16})_{16}$	+2 redox-inactive	12.80	Bi-$O_{close\ to\ VBi}$=2.2 Å ∠F_{eq}-Mn-F_{eq}=159°-173°

Towards off-stoichiometry:

The evolution of the lattice parameters followed by in-situ high temperature XRD is shown on the Fig.3a. It shows the expected lattice dilatation up ~300°C after which the *c*-lattice gets slightly contracted together with the F^- removal and structural collapse discussed below. Minor temperature shifts occur between the various samples, depending on the impurities in presence, and their reactivity with the main Aurivillius phase. For instance, for Sample A, we found a large amount of Bi_2SiO_5 decomposition product, in agreement with small grain SiO_2 byproduct, transported by the fluorine during the synthesis. The reaction benefits further by the good mixing of the SiO_2 particles with the main phase. Following the compounds decomposition by thermogravimetric analysis (TGA) can theoretically provide information about the quantity of fluoride released by hydrolysis of the compound, as well as the oxidation state of the manganese center. To access these two metrics the decomposition under air and nitrogen was investigated (Fig.3b); in both cases, water was purposefully added to the carrier gas (~ 20% RH @25°C corresponding to a dew point of ~ 1°C) to favor the hydrolysis. Note that analysis under dry conditions led to mass losses much higher than expected, most probably due to the sublimation of fluoride species such as BiF_3.

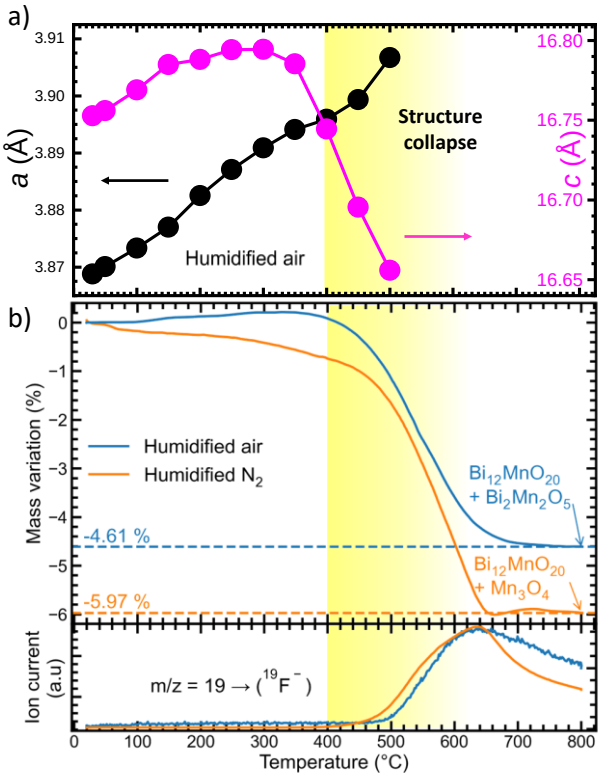

Figure 3: $Bi_2O_2MnF_4$. a) Lattice parameters vs. temperature under air with lattice contraction and structure collapse, coinciding with the F^- removal. b) TGA in humidified air (blue) and N_2 (orange). The bottom graphs show the ion currents for m/z = 19 corresponding to F^- measured in the coupled mass spectroscopy.

TGA of the ~ 75% pure large batches (Sample A) being meaningless, we used nearly-single phase material (Sample B). It was prepared at higher temperature using three cycles of induction-heating/grinding/pelletization with the temperature of the Ta-tube inductor estimated at 750 – 800 °C. The secondary phases MnF_2 (0.12 wt.%) and Mn_3O_4 (0.41 wt.%) have been quantified by Rietveld refinement. The refined lattice parameters (a, b = 3.8651(2) Å, c = 16.681(1) Å) show a ~ 0.4% shortening of the c-lattice parameter compared to the previous ones which suggest stoichiometric deviation in such samples. Despite being partially hidden by the ferrimagnetic signature of the Mn_3O_4 impurity, the ordering temperature T_N = 19.8 K is unchanged compared to the stoichiometric compound. This is an indication of the sole presence of the Mn^{2+} cations, the most stable oxidation state in a F^--rich coordination.

The evolution of the TGA curves of sample B under humidified air and nitrogen (Fig.3b) shows minor evolution of the mass up to 450°C. Here, the slight mass increase under air and mass decrease under nitrogen suggests a weak redox related behavior, followed by the rapid hydrolysis of the compound evidenced by the detection of HF (m/z = 19 and 20) with a coupled mass spectrometer. The decomposition products, post TGA, were identified by XRPD as a mixture of $Bi_{12}MnO_{20}$ + Mn_3O_4 (-5.97 wt.% loss) and $Bi_{12}MnO_{20}$ + $BiMn_2O_5$ (-4.61 wt.% loss) under wet-nitrogen and wet-air respectively. Rietveld refinements of the patterns (Fig.S4), using an estimated 10 µm particle size for Brindley microabsorption corrections [27] give mass fractions consistent with the initial stoichiometry. Furthermore, the complete removal of fluorine was verified by semi-quantitative EDX analysis with a Bi/F ratio evolving from 1.84 on the pristine sample to 0.07 post TGA.

The mass change related to several stoichiometric hypotheses, *i.e.* ideal stoichiometry, substitution of fluorine by oxygen atoms, bismuth vacancies, etc. are listed in Table 2.

i) The total mass losses under both atmospheres, -4.61% (air) and -5.97% (nitrogen), are much lower than the expected, -5.42% and -6.35%, for a perfectly stoichiometric $Bi_2O_2MnF_4$ which validates slight deviations from the ideal stoichiometry. *ii*) Bismuth vacancies as observed in

$Bi_{2-x}O_2FeF_4$ [11] or compensated by F^- for $O^{2-}_{(Bi2O2)\text{-layer}}$ substitution would result in exaggerated mass losses after fluorine removal. *iii*) F^- substitution by O^{2-} species would require more than 25% of substitution in the perovskite slabs but significantly oxidize manganese, contradictory to our magnetic measurements. *iv*) Hence, the most probable type of defect is the substitution of one F^- by ½ O^{2-} and ½ of a vacancy on the perovskite anionic sublattice. A formula close to *v*) $Bi_2O_2MnF_{3.6}O_{0.2}\square_{0.2}$, *i.e.* 5% vacancies, can be derived from the losses observed in the experiment under air and nitrogen. This defect was investigated by DFT and corresponds to a moderate energy cost of 5.06 eV/16f.u. which may be accommodated during our high temperature route, as used for Sample B.

Table 2: Possible composition of the synthesized Mn Aurivillius and theoretical mass loss during the TGA in air or N_2. The experimental losses are -4.61% (air) and -5.97% (nitrogen).

Starting stoichiometry	Atm.	Final stoichiometry	Calc. mass variation
i) $Bi_2O_2Mn^{2+}F_4$	N_2	0.167 $Bi_{12}MnO_{20}$ + 0.278 Mn_3O_4	-6.35%
	Air	0.130 $Bi_{12}MnO_{20}$ + 0.435 $BiMn_2O_5$	-5.42%
ii) $Bi_{1.9}\square_{0.1}O_2Mn^{2.3+}F_4$	N_2	0.158 $Bi_{12}MnO_{20}$ + 0.281 Mn_3O_4	-7.03%
	Air	0.122 $Bi_{12}MnO_{20}$ + 0.439 $BiMn_2O_5$	-6.06%
ii) $Bi_{1.9}\square_{0.1}O_{1.7}F_{0.3}Mn^{2+}F_4$	N_2	0.158 $Bi_{12}MnO_{20}$ + 0.281 Mn_3O_4	-7.18%
	Air	0.122 $Bi_{12}MnO_{20}$ + 0.439 $BiMn_2O_5$	-6.21%
iii) $Bi_2O_2Mn^{2.25+}F_3O$	N_2	0.167 $Bi_{12}MnO_{20}$ + 0.278 Mn_3O_4	-5.86%
	Air	0.130 $Bi_{12}MnO_{20}$ + 0.435 $BiMn_2O_5$	-4.93%
iv) $Bi_2O_2Mn^{2+}F_{3.8}O_{0.1}\square_{0.1}$	N_2	0.167 $Bi_{12}MnO_{20}$ + 0.278 Mn_3O_4	-6.00%
	Air	0.130 $Bi_{12}MnO_{20}$ + 0.435 $BiMn_2O_5$	-5.06%
***v*) $Bi_2O_2Mn^{2+}F_{3.6}O_{0.2}\square_{0.2}$**	**N_2**	**0.167 $Bi_{12}MnO_{20}$ + 0.278 Mn_3O_4**	**-5.63%**
	Air	**0.130 $Bi_{12}MnO_{20}$ + 0.435 $BiMn_2O_5$**	**-4.70%**

Magnetic Properties:

Magnetometry: The magnetic and thermodynamic properties $\chi(T)$, $\chi^{-1}(T)$ and $M(H)$ at T = 30 K and 2 K are shown on Fig.4 for the Sample (A) with 75.3 wt.% purity also used for NPD and SXRD experiments after mass correction of the SiO_2 impurity. After normalization, the Curie-Weiss law fitted in the 60-400 K range returns μ_{eff} = 5.94 μ_B/Mn and Θ_{CW} = -60.4 K. The effective moment is close to the spin-only value for S = 5/2. In the mean field approximated model, the Θ_{CW} value returns $J_{intra,mean\ field}/k_B = 3\cdot\Theta_{CW}/(z\cdot S(S+1))$ = -5.2 K using the number of in-plane neighbors z = 4 and assuming weak inter-layer spin exchanges, as reported for the M = Fe and Ni compounds. Below T_N = 19.8 K, $\chi(T)$ continues increasing, but differently from a paramagnetic-tail and it is assigned to a short-range ordering contribution.

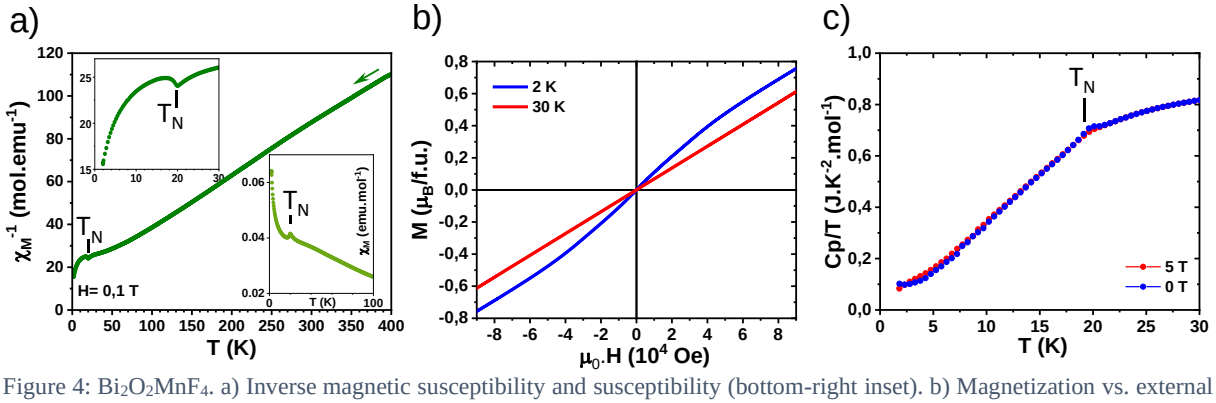

Figure 4: $Bi_2O_2MnF_4$. a) Inverse magnetic susceptibility and susceptibility (bottom-right inset). b) Magnetization vs. external magnetic field. c) Heat capacity measurement. T_N = 19.8 K.

Contrarily to the M = Co, Ni, Mn compounds, no ZFC/FC divergence occurs, in agreement with a colinear antiferromagnetic behavior, as expected for Mn^{2+} (S=5/2, L=0). The antiferromagnetic ordering appears fragile as the magnetization at 2 K and $\mu_0 \cdot H$ = 9 T is 0.76 μ_B/Mn, ~ 1/5th of the expected value for the saturated magnetization M_s.

Exchange couplings by DFT: We evaluated the two spin exchange parameters J_{intra} (in-plane Mn-F-Mn) and J_{inter} (shortest Mn-Mn across the $[Bi_2O_2]^{2+}$ spacers) by energy-mapping analysis based on GGA+U calculations using the fully ordered *ideal*$_{P\text{-}1}$ model whose perovskite layers are shown in Fig.1h. We used three *up/down* spin-polarized configurations similar to those used for M = Fe and Ni.[10] U was varied to 2, 4, and 6 eV with results given in Table S4. As discussed above, our experimental Θ_{CW} (=60.4 K, $J_{mean\text{-}field}$ = 5.2 K) match the calculations with U = 4 eV (J_{intra} = 4.73 K, AFM). The J_{inter} value of 0.02 K (AFM) highlights a pronounced anisotropic 2D topology of magnetic exchanges. It is clear from the Cp/T(T) plot shown in Fig.4c that this 2D-scenario prevails, leading to a very weak signature of T_N due to significant *in-plane* contributions above. Preliminary dielectric measurements on a dense pellet (~300 μm thick) did not show any anomaly at T_N, refuting significant magneto-electric couplings. These results will be published elsewhere. The relatively weak J_{intra} value compared to the M = Ni and Fe compounds [11] can be understood on the basis of the longer Mn-Mn distance and lower M-F-M super exchange angle, see Table 3. It is in agreement with the smaller T_N value of the rock-salt MnO (T_N = 122 K)[28] compared to those of NiO (T_N = 523 K)[28], CoO (T_N = 291 K)[28] and FeO (T_N = 198 K).[28] Indeed, besides geometrical considerations, as Moriya suggested, it is likely, that the d^5 exchange integral is somewhat less extended than for d^8, d^7, and d^6 ions.[29]

Table 3: $Bi_2O_2MF_4$. Experimental magnetic parameters from Curie-Weiss fit and exchange interactions J_{intra} from DFT+U calculations. The values for Fe, Co, and Ni are taken from previous publication.[11]

Formula	d_{avg}(M-M)/Å	$\mu_{eff,CW}/M^{2+}$	θ_{CW}/K	$J_{intra,mean\ field}/k_B$	J_{intra}/k_B
$Bi_2O_2MnF_4$	3.869	5.94	-60.4	-5.18 K	+4.73 K (U=4eV)
$Bi_{2-x}O_2FeF_4$	3.841	5.52(5)	-338(1)	-42.25 K	+33.81 K (U=5eV)
$Bi_2O_2CoF_4$	3.843	5.62	-142	-28.4 K	-
$Bi_2O_2NiF_4$	3.824	-	-	-	+54.7 K (U=5eV)

Magnetic Structure: It was refined from the 5-30 K NPD difference pattern, see Fig.5a. The magnetic peaks can be indexed with the **k** = (½ ½ 0) propagation vector. Group theory analysis combined with our magnetic pattern indicates the magnetic mX_2^+ irreducible representation as active, corresponding to the *Cmca*.1'$_A$ (64.480) magnetic space group. It splits the Mn2 position into two individual magnetic orbits at (0,0,0) and (½,½,½) respectively with 0,0,M_z moments along the *c*-axis. After refining at constant scale factor (as from the 30 K NPD data) and constraining a unique moment for both antiparallel orbits, the refinement returns M_z = 3.8(2) μ_B/Mn with $R_{magn.}$=8.04%. In contrast to the non-colinear magnetic structures for the M = Fe, Ni, and Co cases (Fig.5c-e), Mn^{2+} moments align along the *c*-axis antiparallel (*G*-type structure), showing the absence of orbital contribution for which the spin moment is poorly sensitive to the local ligand orbital overlap, but lies along a crystallographic direction, see Fig.5b.

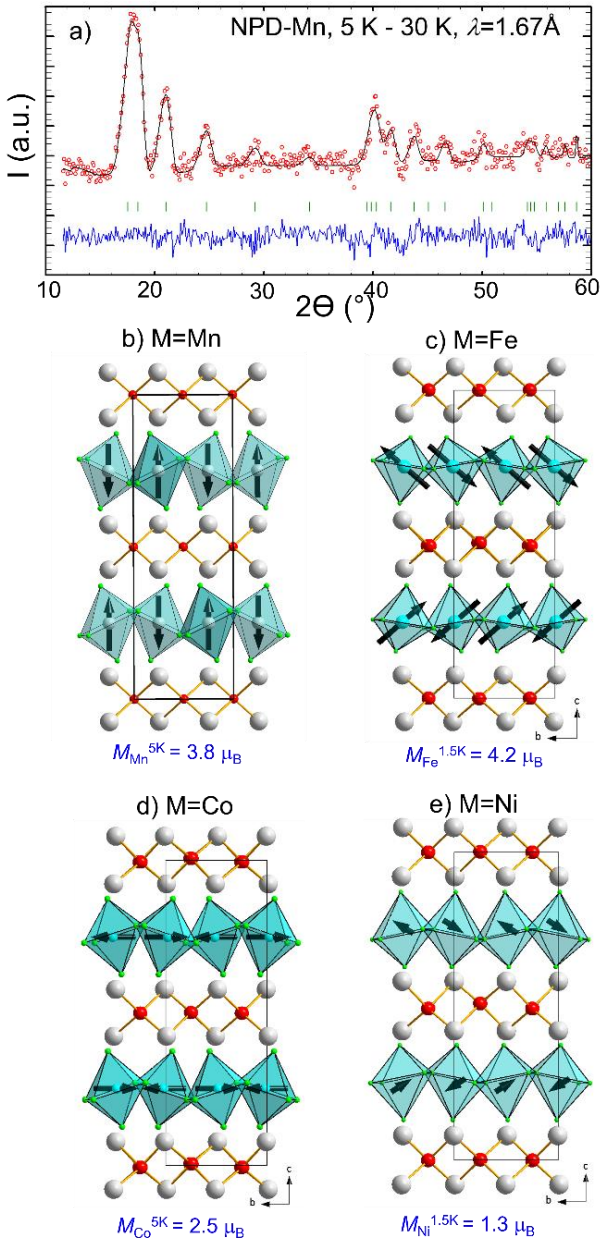

Figure 5: a) Magnetic Rietveld refinement against the difference neutron powder diffraction data 5 K - 30 K of $Bi_2O_2MnF_4$ recorded on the PEARL diffractometer (λ = 1.67 Å). b) Refined magnetic structure. c-e) Magnetic structures of the other 3*d* transition metal members of the family.[11,12]

Ionic mobility:

The Aurivillius structure, allowing the presence of many defects, in particular the possible presence of anionic vacancies on the perovskite framework as proposed in this article based on thermogravimetric measurements, could potentially result in high ionic mobility. The transport properties of $Bi_2O_2MnF_4$ were therefore investigated up to 400°C, since higher temperatures trigger severe decomposition of the structure. Despite the small temperature range of the measurement, a change in behavior occurs at 300°C. Below this temperature, in addition of the 45° slope at low frequency, typical of the limitation due to ionic diffusion, two semi-circles can clearly be identified on the Nyquist representation of the electrochemical impedance spectra (EIS) as shown at 202°C in Fig.6a. The situation above 300°C is not as clear: due to the overlap of the two low frequency contributions a significant deviation from the 45° slope of the electrode response is observed (Fig.6b). The whole temperature range can be modelled with the

equivalent circuit presented in Fig.6c. The thermal evolution follows the standard Arrhenius behavior below 300°C and early signs of the structures hydrolysis are affecting the measurement at higher temperatures.

The high frequency semi-circle was modeled using a resistor in parallel with a constant phase element $(R/CPE)_{Ion}$. It was associated to the ionic mobility within the structure, most likely purely fluoride given the low temperature and the low value of the activation energy $E_{a,Ion}$ =0.65 eV. The derived ionic conductivity would be modest with ~ 1 mS cm^{-1} at 300°C, *i.e.* slightly higher than the doped CaF_2 compositions but three orders of magnitude lower than the best fluoride ion conductors such as $PbSnF_4$.[30] The very depressed semi-circle at intermediate frequencies was also modeled using a resistor in parallel with a constant phase element $(R/CPE)_{Ox}$. It was tentatively associated to the chemical impedance due to the low-temperature oxidation of $Bi_2O_2MnF_4$ as evidenced by the difference in mass loss under air and nitrogen (Fig.3b). Moreover, this is further strengthened considering the sharp increase in resistance at 300°C, corresponding to the end of the mass gain observed by TGA. Further experiments under controlled oxygen partial pressure would be required to fully support this hypothesis.

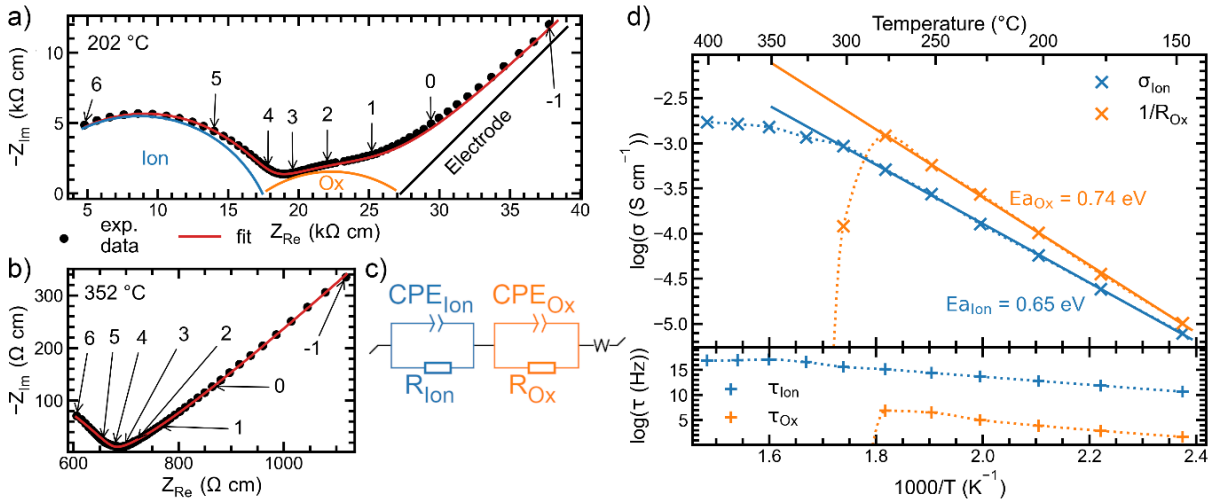

Figure 6: $Bi_2O_2MnF_4$. Nyquist plots of the EIS measurements at a) 202°C and b) 352°C. c) Equivalent circuit used to fit the data, the blue $(R/CPE)_{Ion}$ element corresponds to ionic transport and the orange $(R/CPE)_{Ox}$ element corresponds to the oxidation of the material. d) Electric conductivity (top) and associated time constants (bottom)..The label Ox refers to the weak oxidation of of the sample suggested by TGA under air.

Conclusions:

The Aurivillius family of compounds have been widely studied for their ionic-transport,[31–33] ferroelectric,[12,34,35] and photocatalytic behaviors.[36,37] Recent advancements in the synthesis of hybrid oxyfluoride Aurivillius phases have demonstrated the potential to tailor their structural and electronic properties by incorporating transition metal cations such as iron and cobalt. In this context, the discovery of a new Aurivillius phase with a single perovskite layer (n = 1) incorporating divalent manganese (Mn^{2+}) and fluorine represents a significant step forward in this family of compounds. Overall, it opens wide perspectives on the possible chemical diversification to an extended variety of 3*d*, 4*d* and 5*d* transition metals with sizeable oxidation numbers.

Structurally, this Mn-based Aurivillius shows evidence of both an ideal stoichiometry $[Bi_2O_2][MnF_4]$ and strongly equatorially and apically tilted octahedra. However, only SRO correlations exist in its perovskite sub-units. Thus, it offers an intriguing avenue to explore the interplay of the electronic configurations of the metal and sizeable lattice defects. For d^5 Mn^{2+} ions, we concluded that local distortions without significant energy penalties create convenient

"*scissor*"-points between short range ordered domains with various octahedral sequences and tilts. Other anti-site and ionic deficient defects have been computed and clues for the most "stable" ones have been matched either by HAADF images (O for F exchange in between the fluorite and perovskite sub-units), or by thermogravimetric analysis on "high-temperature" samples (fluorine replaced by oxygen and vacancies). These results highlight the importance of controlled synthesis conditions, such as solvothermal or soft chemical routes, for stabilizing various defective variations of ideal Aurivillius oxyfluorides. Moreover, the introduction of S=5/2, L=0 Mn^{2+} ions into the Aurivillius framework expands the compositional landscape of this family, paving the way for further exploration of their magnetic phenomena. $[Bi_2O_2][MnF_4]$ shows an AFM structure similar to what is observed for the other M = $Fe^{2+/3+}$, Co^{2+}, Ni^{2+} analogs, but within a perfectly colinear spin alignment, which finally differs from the other cations where partially unfrozen spin-orbit couplings (SOC) generate spin canting and weak ferromagnetism. Hence, the Aurivillius M^{2+} oxyfluorides finally cover a full range of magnetocrystalline anisotropy, which leaves questions about the mixed M/M' cationic systems to be further investigated. The compound shows moderate ionic conductivity up to 300°C. Above this temperature the thermal instability of $Bi_2O_2MnF_4$ does not allow stable electrochemistry in air. It might still be interesting for catalytic processes at moderate temperatures which still are to be studied.

Access Code CCDC 2446163 contains the supplementary crystallographic data for this paper. These data can be obtained free of charge via www.ccdc.cam.ac.uk/data_request/cif, or by emailing data_request@ccdc.cam.ac.uk, or by contacting The Cambridge Crystallographic Data Centre, 12 Union Road, Cambridge CB2 1EZ, UK; fax: +44 1223 336033.

Associated content:

Supporting information: Details of the powder structure refinement of sample A (lattice parameters, atomic positions, anisotropic displacement parameters, and interatomic distances). Neutron powder refinement including impurity phase determination and cell parameters of the main phase. EDX mapping analysis on sample B. Information regarding the examination of possible stacking faults investigated using the FAULTS program.[15] Magnetic exchange parameters derived from DFT+U calculations using different U values. TGA results on sample B under air and nitrogen atmosphere. DFT+U lattice parameters compared to the experimental parameters transferred to the corresponding unit cells. Pictures of the used defect structures for DFT+U calculations.

Acknowledgements:

The Fonds Européen de Développement Régional, CNRS, Région Hauts-de-France, and Ministère de l'Education Nationale de l'Enseignement Supérieur et de la Recherche are acknowledged for funding the X-ray diffractometers and PPMS system. The Région Hauts-de-France supported the funding of J.W. PhD thesis. Laurence Burylo (XRD) and Claire Minaud (magn. measurements) are thanked for their experimental help. Granted beam time at ILL is appreciated as well (DOI: 10.5291/ILL-DATA.5-31-3019). The project CEFIPRA Project 7108-2 ENUMERATED is thanked for dielectric measurements.

References:

(1) Kageyama, H.; Hayashi, K.; Maeda, K.; Attfield, J. P.; Hiroi, Z.; Rondinelli, J. M.; Poeppelmeier, K. R. Expanding Frontiers in Materials Chemistry and Physics with Multiple Anions. *Nat. Commun.* **2018**, *9* (1), 772. https://doi.org/10.1038/s41467-018-02838-4.

(2) Hyrondelle, H.; Suchomel, M. R.; Rodriguez, V.; Durand, E.; Millot, Y.; Duttine, M.; Demourgues, A. Decoding Anionic Organization of Hydroxide-Fluorides in a Diaspore-Type Network. *Inorg. Chem.* **2025**, *64* (4), 1677–1689. https://doi.org/10.1021/acs.inorgchem.4c03794.
(3) Aurivillius, B. The structure of Bi_2NbO_5F and isomorphous compounds. *Ark. För Kemi* **1952**, *4*, 39–47.
(4) Akopjan, A. V.; Serov, T. V.; Dolgikh, V. A.; Ardaschnikova, E. I.; Lightfoot, P. A New Anion Conductive Bismuth–Vanadium Oxyfluoride. *J. Mater. Chem.* **2002**, *12* (5), 1490–1494. https://doi.org/10.1039/B201049F.
(5) Needs, R. L.; Dann, S. E.; Weller, M. T.; Cherryman, J. C.; Harris, R. K. The Structure and Oxide/Fluoride Ordering of the Ferroelectrics $Bi_2TiO_4F_2$ and Bi_2NbO_5F. *J. Mater. Chem.* **2005**, *15* (24), 2399–2407. https://doi.org/10.1039/B502499D.
(6) Giddings, A. T.; Scott, E. A. S.; Stennett, M. C.; Apperley, D. C.; Greaves, C.; Hyatt, N. C.; McCabe, E. E. Symmetry and the Role of the Anion Sublattice in Aurivillius Oxyfluoride $Bi_2TiO_4F_2$. *Inorg. Chem.* **2021**, *60* (18), 14105–14115. https://doi.org/10.1021/acs.inorgchem.1c01933.
(7) Ismailzade, I. H.; Ravez, J. $Bi_2TiO_4F_2$—a New One-Layer Perovskite-like Ferroelectric. *Ferroelectrics* **1978**, *21* (1), 423–424. https://doi.org/10.1080/00150197808237285.
(8) Chen, J.; Liu, H.; Zhu, L.; Fu, Z.; Lu, Y. One-Pot Synthesis of $Bi_2TiO_4F_2$/BiOBr Ferroelectric Heterostructure for Photocatalytic Oxygen Evolution. *J. Alloys Compd.* **2021**, *873*, 159847. https://doi.org/10.1016/j.jallcom.2021.159847.
(9) Katayama, T.; Chikamatsu, A.; Hirayama, M. Antiferroelectric Behavior in Mixed-Anion $Bi_2TiO_4F_2$ Induced by Rotation of TiO_3F_3 Octahedra. *Adv. Funct. Mater.* **2025**, *n/a* (n/a), 2500489. https://doi.org/10.1002/adfm.202500489.
(10) Benomar, S.; Bousquet, E.; Djani, H. Multianion Induced Out-of-Plane Proper Polarization in Oxyfluoride Aurivillius $Bi_2TiO_4F_2$. *J. Phys. Chem. Solids* **2022**, *167*, 110720. https://doi.org/10.1016/j.jpcs.2022.110720.
(11) Mentré, O.; Juárez-Rosete, M. A.; Colmont, M.; Ritter, C.; Fauth, F.; Duttine, M.; Huvé, M.; Terryn, C.; Duffort, V.; Arévalo-López, Á. M. All-Magnetic Slabs and Multiferroism in $(Bi_{2-x}O_2)(MF_4)$ Aurivillius Oxyfluorides (M = Fe and Ni). *Chem. Mater.* **2022**, *34* (12), 5706–5716. https://doi.org/10.1021/acs.chemmater.2c01213.
(12) Scott, E. A. S.; Mitoudi Vagourdi, E.; Johnsson, M.; Cascos, V.; John, F.; Pickup, D.; Chadwick, A. V.; Djani, H.; Bousquet, E.; Zhang, W.; Halasyamani, P. S.; McCabe, E. E. $Bi_2CoO_2F_4$–A Polar, Ferrimagnetic Aurivillius Oxide-Fluoride. *Chem. Mater.* **2022**, *34* (21), 9775–9785. https://doi.org/10.1021/acs.chemmater.2c02745.
(13) Mitoudi Vagourdi, E.; Müllner, S.; Lemmens, P.; Kremer, R. K.; Johnsson, M. Synthesis and Characterization of the Aurivillius Phase $CoBi_2O_2F_4$. *Inorg. Chem.* **2018**, *57* (15), 9115–9121. https://doi.org/10.1021/acs.inorgchem.8b01118.
(14) van Eijck, L.; Cussen, L. D.; Sykora, G. J.; Schooneveld, E. M.; Rhodes, N. J.; van Well, A. A.; Pappas, C. Design and Performance of a Novel Neutron Powder Diffractometer: PEARL at TU Delft. *J. Appl. Crystallogr.* **2016**, *49* (5), 1398–1401. https://doi.org/10.1107/S160057671601089X.
(15) Casas-Cabanas, M.; Reynaud, M.; Rikarte, J.; Horbach, P.; Rodríguez-Carvajal, J. FAULTS: A Program for Refinement of Structures with Extended Defects. *J. Appl. Crystallogr.* **2016**, *49* (6), 2259–2269. https://doi.org/10.1107/S1600576716014473.
(16) Kresse, G.; Furthmüller, J. Efficiency of Ab-Initio Total Energy Calculations for Metals and Semiconductors Using a Plane-Wave Basis Set. *Comput. Mater. Sci.* **1996**, *6* (1), 15–50. https://doi.org/10.1016/0927-0256(96)00008-0.
(17) Kresse, G.; Hafner, J. Ab Initio Molecular-Dynamics Simulation of the Liquid-Metal--Amorphous-Semiconductor Transition in Germanium. *Phys. Rev. B* **1994**, *49* (20), 14251–14269. https://doi.org/10.1103/PhysRevB.49.14251.
(18) Kresse, G.; Furthmüller, J. Efficient Iterative Schemes for Ab Initio Total-Energy Calculations Using a Plane-Wave Basis Set. *Phys. Rev. B* **1996**, *54* (16), 11169–11186. https://doi.org/10.1103/PhysRevB.54.11169.
(19) Perdew, J. P.; Burke, K.; Ernzerhof, M. Generalized Gradient Approximation Made Simple. *Phys. Rev. Lett.* **1996**, *77* (18), 3865–3868. https://doi.org/10.1103/PhysRevLett.77.3865.
(20) Blöchl, P. E. Projector Augmented-Wave Method. *Phys. Rev. B* **1994**, *50* (24), 17953–17979. https://doi.org/10.1103/PhysRevB.50.17953.
(21) Dudarev, S. L.; Botton, G. A.; Savrasov, S. Y.; Humphreys, C. J.; Sutton, A. P. Electron-Energy-Loss Spectra and the Structural Stability of Nickel Oxide: An LSDA+U Study. *Phys. Rev. B* **1998**, *57* (3), 1505–1509. https://doi.org/10.1103/PhysRevB.57.1505.
(22) Monkhorst, H. J.; Pack, J. D. Special Points for Brillouin-Zone Integrations. *Phys. Rev. B* **1976**, *13* (12), 5188–5192. https://doi.org/10.1103/PhysRevB.13.5188.
(23) Brese, N. E.; O'Keeffe, M. Bond-Valence Parameters for Solids. *Acta Crystallogr. B* **1991**, *47* (2), 192–197. https://doi.org/10.1107/S0108768190011041.
(24) Burley, G. A.; Taylor, R. Manganese Trifluoride. In *Encyclopedia of Reagents for Organic Synthesis*; John Wiley & Sons, Ltd, 2004. https://doi.org/10.1002/047084289X.rn00411.
(25) Zhong, C.; Tassel, C.; Kato, D.; Ogawa, K.; Niwa, K.; Tomita, O.; Ito, Y.; Kawaguchi, S.; Hasegawa, M.; Abe, R.; Kageyama, H. Decompression-Induced In-Plane Lone Pair Electrons in BiSF Synthesized under High Pressure. *Chem. Mater.* **2024**, *36* (9), 4495–4501. https://doi.org/10.1021/acs.chemmater.4c00114.
(26) Zhang, Y.; Yamamoto, T.; Green, M. A.; Kageyama, H.; Ueda, Y. Interlayer Communication in Aurivillius Vanadate to Enable Defect Structures and Charge Ordering. *Inorg. Chem.* **2015**, *54* (22), 10925–10933. https://doi.org/10.1021/acs.inorgchem.5b01964.
(27) Brindley, G. W. XLV. The Effect of Grain or Particle Size on x-Ray Reflections from Mixed Powders and Alloys, Considered in Relation to the Quantitative Determination of Crystalline Substances by x-Ray Methods. *Lond. Edinb. Dublin Philos. Mag. J. Sci.* **1945**. https://doi.org/10.1080/14786444508520918.
(28) Roth, W. L. Magnetic Structures of MnO, FeO, CoO, and NiO. *Phys. Rev.* **1958**, *110* (6), 1333–1341. https://doi.org/10.1103/PhysRev.110.1333.

(29) Anderson, P. W. Theory of Magnetic Exchange Interactions:Exchange in Insulators and Semiconductors. In *Solid State Physics*; Seitz, F., Turnbull, D., Eds.; Academic Press, 1963; Vol. 14, pp 99–214. https://doi.org/10.1016/S0081-1947(08)60260-X.
(30) Patro, L. N.; Hariharan, K. Fast Fluoride Ion Conducting Materials in Solid State Ionics: An Overview. *Solid State Ion.* **2013**, *239*, 41–49. https://doi.org/10.1016/j.ssi.2013.03.009.
(31) Kendall, K. R.; Navas, C.; Thomas, J. K.; zur Loye, H.-C. Recent Developments in Oxide Ion Conductors: Aurivillius Phases. *Chem. Mater.* **1996**, *8* (3), 642–649. https://doi.org/10.1021/cm9503083.
(32) Pham, A.-Q.; Puri, M.; DiCarlo, J. F.; Jacobson, A. J. Oxide Ion Conductivity of the New Aurivillius Phase $(Bi_2O_2)(NaNb_2O_{6.5})$. *Solid State Ion.* **1994**, *72*, 309–313. https://doi.org/10.1016/0167-2738(94)90165-1.
(33) Beg, S.; Al-Alas, A.; Al-Areqi, N. A. S. Layered Aurivillius Compound: Synthesis, Characterization and Electrical Properties. *J. Alloys Compd.* **2010**, *504* (2), 413–419. https://doi.org/10.1016/j.jallcom.2010.05.133.
(34) Scott, J. F. Room-Temperature Multiferroic Magnetoelectrics. *NPG Asia Mater.* **2013**, *5* (11), e72–e72. https://doi.org/10.1038/am.2013.58.
(35) Djani, H.; Bousquet, E.; Kellou, A.; Ghosez, P. First-Principles Study of the Ferroelectric Aurivillius Phase Bi_2WO_6. *Phys. Rev. B* **2012**, *86* (5), 054107. https://doi.org/10.1103/PhysRevB.86.054107.
(36) Jiang, B.; Zhang, P.; Zhang, Y.; Wu, L.; Li, H.; Zhang, D.; Li, G. Self-Assembled 3D Architectures of $Bi_2TiO_4F_2$ as a New Durable Visible-Light Photocatalyst. *Nanoscale* **2012**, *4* (2), 455–460. https://doi.org/10.1039/C1NR11331C.
(37) Lei, S.; Cheng, D.; Gao, X.; Fei, L.; Lu, W.; Zhou, J.; Xiao, Y.; Cheng, B.; Wang, Y.; Huang, H. A New Low-Temperature Solution Route to Aurivillius-Type Layered Oxyfluoride Perovskites Bi_2MO_5F (M = Nb, Ta) as Photocatalysts. *Appl. Catal. B Environ.* **2017**, *205*, 112–120. https://doi.org/10.1016/j.apcatb.2016.12.029.

For Table of Contents Only